The VIMOS-VLT Deep Survey: evolution in the halo occupation number since $z \sim 1$[★]

U. Abbas,[1,2]† S. de la Torre,[1,3,4] O. Le Fèvre,[1] L. Guzzo,[3,5,6] C. Marinoni,[7]
B. Meneux,[5,8] A. Pollo,[9,10] G. Zamorani,[11] D. Bottini,[4] B. Garilli,[4] V. Le Brun,[1]
D. Maccagni,[4] R. Scaramella,[12,13] M. Scodeggio,[4] L. Tresse,[1] G. Vettolani,[12]
A. Zanichelli,[12] C. Adami,[1] S. Arnouts,[1,14] S. Bardelli,[11] M. Bolzonella,[11] A. Cappi,[11]
S. Charlot,[6,15] P. Ciliegi,[11] T. Contini,[16] S. Foucaud,[17] P. Franzetti,[4] I. Gavignaud,[18]
O. Ilbert,[19] A. Iovino,[3] F. Lamareille,[11] H. J. McCracken,[15,20] B. Marano,[21] A. Mazure,[1]
R. Merighi,[11] S. Paltani,[22,23] R. Pellò,[16] L. Pozzetti,[11] M. Radovich,[24] D. Vergani,[4]
E. Zucca,[11] M. Bondi,[12] A. Bongiorno,[5] J. Brinchmann,[25] O. Cucciati,[1,3] L. de Ravel,[1]
L. Gregorini,[12] E. Perez-Montero,[16] Y. Mellier[15,20] and P. Merluzzi[24]

[1]*Laboratoire d'Astrophysique de Marseille, UMR 6110 CNRS-Université de Provence, 38 rue Frederic Joliot Curie, F-13388 Marseille Cedex 13, France*
[2]*INAF-Osservatorio Astronomico di Torino, Strada Osservatorio 20, I-10025 Pino Torinese, Italy*
[3]*INAF-Osservatorio Astronomico di Brera, Via Brera 28, I-20021 Milan, Italy*
[4]*IASF-INAF, Via Bassini 15, I-20133 Milano, Italy*
[5]*Max Planck Institut für Extraterrestrische Physik (MPE), Giessenbachstrasse 1, D-85748 Garching bei München, Germany*
[6]*Max Planck Institut für Astrophysik, D-85741 Garching, Germany*
[7]*Centre de Physique Théorique, UMR 6207 CNRS-Université de Provence, F-13288 Marseille, France*
[8]*Universitätssternwarte München, Scheinerstrasse 1, D-81679 München, Germany*
[9]*The Andrzej Soltan Institute for Nuclear Studies, ul. Hoza 69, 00-681 Warszawa, Poland*
[10]*Astronomical Observatory of the Jagiellonian University, ul. Orla 171, PL-30-244 Kraków, Poland*
[11]*INAF-Osservatorio Astronomico di Bologna, Via Ranzani 1, I-40127 Bologna, Italy*
[12]*IRA-INAF, Via Gobetti 101, I-40129 Bologna, Italy*
[13]*INAF-Osservatorio Astronomico di Roma, Via di Frascati 33, I-00040 Monte Porzio Catone, Italy*
[14]*Canada France Hawaii Telescope Corporation, Mamalahoa Hwy, Kamuela, HI 96743, USA*
[15]*Institut d'Astrophysique de Paris, UMR 7095, 98 bis Bvd Arago, F-75014 Paris, France*
[16]*Laboratoire d'Astrophysique de Toulouse/Tabres (UMR5572), CNRS, Université Paul Sabatier - Toulouse III, Observatoire Midi-Pyrénées, 14 av. E. Belin, F-31400 Toulouse, France*
[17]*School of Physics & Astronomy, University of Nottingham, University Park, Nottingham NG7 2RD*
[18]*Astrophysical Institute Potsdam, An der Sternwarte 16, D-14482 Potsdam, Germany*
[19]*Institute for Astronomy, 2680 Woodlawn Dr., University of Hawaii, Honolulu, HI 96822, USA*
[20]*Observatoire de Paris, LERMA, 61 Avenue de l'Observatoire, F-75014 Paris, France*
[21]*Università di Bologna, Dipartimento di Astronomia, Via Ranzani 1, I-40127 Bologna, Italy*
[22]*Integral Science Data Centre, ch. d'Écogia 16, CH-1290 Versoix, Switzerland*
[23]*Geneva Observatory, ch. des Maillettes 51, CH-1290 Sauverny, Switzerland*
[24]*INAF-Osservatorio Astronomico di Capodimonte, Via Moiariello 16, I-80131 Napoli, Italy*
[25]*Centro de Astrofísica da Universidade do Porto, Rua das Estrelas, P-4150-762 Porto, Portugal*

ABSTRACT

We model the evolution of the mean galaxy occupation of dark matter haloes over the range $0.1 < z < 1.3$, using the data from the VIMOS-VLT Deep Survey. The galaxy projected correlation function $w_p(r_p)$ was computed for a set of luminosity-limited subsamples and fits to its shape were obtained using two variants of halo occupation distribution (HOD) models. These provide us with a set of best-fitting parameters, from which we obtain the average

---

mass of a halo and average number of galaxies per halo. We find that after accounting for the evolution in luminosity and assuming that we are largely following the same population, the underlying dark matter halo shows a growth in mass with decreasing redshift as expected in a hierarchical structure formation scenario. Using two different HOD models, we see that the halo mass grows by 90 per cent over the redshift interval $z = [0.5, 1.0]$. This is the first time the evolution in halo mass at high redshifts has been obtained from a single data survey and it follows the simple form seen in N-body simulations with $M(z) = M_0 \, e^{-\beta z}$, and $\beta = 1.3 \pm 0.30$. This provides evidence for a rapid accretion phase of massive haloes having a present-day mass $M_0 \sim 10^{13.5} \, h^{-1} \, \mathrm{M_\odot}$, with a $m > 0.1 M_0$ merger event occurring between redshifts of 0.5 and 1.0. Furthermore, we find that more luminous galaxies are found to occupy more massive haloes irrespective of the redshift. Finally, the average number of galaxies per halo shows little increase from redshift $z \sim 1.0$ to ~ 0.5, with a sharp increase by a factor of ~ 3 from $z \sim 0.5$ to ~ 0.1, likely due to the dynamical friction of subhaloes within their host haloes.

Key words: methods: statistical – surveys – galaxies: high-redshift – large-scale structure of Universe.

1 INTRODUCTION

The correlation function of galaxies is a simple yet powerful tool that allows one to constrain cosmological parameters and models of galaxy formation. Furthermore, with the help of high-redshift surveys, the evolution in the clustering of galaxies allows for a better discrimination between theoretical models degenerate at the present epoch (Peacock 1997).

Until recently, the galaxy correlation function had been thought to follow a power law (Totsuji & Kihara 1969; Peebles 1974; Gott & Turner 1979). Subsequently, a departure from the power law on small scales (of the order 1 to a few Mpc h^{-1}) in the galaxy correlation function was noticed in pioneering surveys of the 1980s (e.g. Guzzo et al. 1991) and has now been fully confirmed by many large and deep galaxy surveys. These consist of various surveys at low and intermediate redshifts ($z \leq 1.5$) such as the Sloan Digital Sky Survey (SDSS; Connolly et al. 2002; Zehavi et al. 2004), 2dF Galaxy Redshift Survey (2dFGRS; Magliocchetti & Porciani 2003), VIMOS-VLT Deep Survey (VVDS; Le Fèvre et al. 2005b; Pollo et al. 2006), Classifying Objects by Medium-Band Observations in 17 Filters (COMBO-17; Phleps et al. 2006), DEEP2 (Coil et al. 2006) and for Lyman break galaxies (LBGs) at high redshifts in the *Subaru/XMM–Newton* Deep Survey (SXDS) and the Great Observatories Origins Deep Survey (GOODS; Ouchi et al. 2005; Lee et al. 2006).

Earliest measures showing a non-power law for the galaxy correlation function were difficult to interpret as they relied heavily upon the angular correlation function, $\omega(\theta)$, at low redshifts (Connolly et al. 2002). This meant an integration over a wide range of galaxy luminosities and redshifts as well as complicated correlations between the statistical errors (Zehavi et al. 2004). This was followed by measurements of the projected correlation function, $w_p(r_p)$, and $\omega(\theta)$ in larger and deeper surveys. It has been seen that the deviation from a power law becomes more pronounced for bright galaxy samples with $L > L_\star$ (Coil et al. 2006; Pollo et al. 2006) and for LBGs at high redshifts (Lee et al. 2006). Likewise, in smoothed particle hydrodynamics (SPH) simulations the luminous and more strongly clustered galaxies show a similar behaviour where the 'kink' is clearer than in the case of the full galaxy sample (Weinberg et al. 2004).

Interestingly enough, the correlation function for dark matter in N-body simulations is well known to be non-adherent to a power law (Jenkins et al. 1998; Kauffmann et al. 1999; Cooray & Sheth 2002 and references therein). The natural question that arises is how biased is the galaxy distribution with respect to the underlying matter distribution? The overall shape of the dark matter correlation function is mostly unaffected as one goes to higher redshifts as seen in SPH simulations (Weinberg et al. 2004) and N-body simulations (Jenkins et al. 1998). This is different to what is seen for high-z galaxies (Ouchi et al. 2005; Lee et al. 2006; Zheng, Coil & Zehavi 2007), where the so-called 'break' is more prominent implying that the biasing of the galaxy distribution on large scales, spatial exclusion of dark matter haloes on small scales, along with a host of other complex physical processes, such as dynamical friction, feedback from supernovae, ram-pressure stripping etc. conspire in a non-trivial way to produce differences in the galaxy correlation function at different redshifts.

The break in the power law can be physically interpreted in the language of the halo model (see Cooray & Sheth 2002 for a detailed review) as the transition between two scales – small scales lying within the halo to those larger than the halo. It is only natural to use a halo-based prescription where galaxies form by the cooling of gas within dark matter haloes (White & Rees 1978), which are bound, virialized clumps of dark matter that are roughly 200 times the background density at that time (Gunn & Gott 1972). The galaxies occupy dark matter haloes following a halo occupation distribution (HOD) model. In turn the HOD fully describes the bias in the distribution of galaxies with respect to the underlying dark matter distribution (Berlind & Weinberg 2002).

The motivation for HOD-based models arose when it was noticed that the clustering of galaxies could be reproduced by populating haloes in semi-analytic models with galaxies following a particular probability distribution (Kauffmann et al. 1999; Benson et al. 2000; Berlind & Weinberg 2002). Furthermore, it has been seen that without the help of a proper halo-based description the strong clustering of red galaxies (at $z \simeq 3$) can be explained by high and unrealistic (anywhere in the range of 70–200 galaxies per halo) occupation numbers to match the observed number density and strong clustering of a small number of high-mass haloes (Zheng 2004).

Recently, several groups have studied the galaxy correlation in light of the HOD models (Magliocchetti & Porciani 2003; van den Bosch, Yang & Mo 2003; Hamana et al. 2004; Ouchi et al. 2005; Zehavi et al. 2005; Conroy, Wechsler & Kravtsov 2006; Phleps et al. 2006; Zheng et al. 2007). Most of these works have mainly concentrated on obtaining best-fitting HOD parameters and consequently the evolution in the HOD and information on the underlying dark matter distribution. In some cases, data from different surveys having different selections were used to study the evolution (Conroy et al. 2007; Zheng et al. 2007). The work in this paper complements and extends these analyses by studying the evolution in the HOD over a redshift range $z \approx 0.1$–1.3 for a variety of luminosity-limited samples but always for data from the same survey, the VVDS. We also study two different HOD models in order to obtain a better understanding on the degeneracies between the various parameters.

The paper is organized as follows. In Section 2 we briefly describe the data used from the VVDS survey. This section is followed by Section 3 giving an outline of the theoretical framework. Section 4 describes the fitting procedure along with the best-fitting parameters obtained for the different models. The estimates for the average halo mass and number of galaxies per halo (galaxy weighted) for the different luminosity-threshold samples are also presented. Finally, Section 5 wraps up with a discussion and conclusion of the results.

Throughout we will assume a flat Λ cold dark matter (ΛCDM) model for which $(\Omega_0, h, \sigma_8) = (0.3, 0.7, 0.9)$ at $z = 0$. Here Ω_0 is the density in units of critical density today, h is the Hubble constant today in units of $100 \, \mathrm{km \, s^{-1} \, Mpc^{-1}}$ and σ_8 describes the rms fluctuations of the initial field evolved to the present time using linear theory and smoothed with a top-hat filter of radius $8 \, \mathrm{Mpc} \, h^{-1}$. All absolute magnitudes are in the AB system.

2 THE VVDS DATA AND ITS ANALYSIS

2.1 Description of the data

The data used in this analysis come from the First Epoch VVDS 0226-04 'Deep' field (hereafter VVDS-Deep). A complete description of the data, survey strategy, data reduction and primary goals can be found in Le Fèvre et al. (2005a). Here we will simply give a short description of the data used.

The VVDS-Deep sample is magnitude limited in the I_{AB} band with $17.5 \leq I_{AB} \leq 24$ and covers an area of $0.49 \, \mathrm{deg^2}$ without any colour or shape restrictions imposed. The spectroscopic observations were taken with the Visible Multiple-Object Spectrograph (VIMOS; Le Fèvre et al. 2003) at the ESO Very Large Telescope (VLT), whereas the Virmos Deep Imaging Survey (VDIS) *BVRI* photometric data (Le Fèvre et al. 2004) was obtained with the wide field 12 k mosaic camera at the Canada–France–Hawaii Telescope (CFHT) and is complete and free from surface brightness selection effects (McCracken et al. 2003).

The sample contains 6582 galaxies with secure redshifts, i.e. known at a confidence level ≥80 per cent. These galaxies have a mean redshift of $z \approx 0.83$. Fig. 1 shows the absolute magnitude of these galaxies as a function of redshift along with the different luminosity-threshold subsamples selected, where the luminosity threshold is assumed to evolve according to the relation $M_B(z) = -1.15z + M_B(z = 0)$. The factor of '−1.15' arises from the redshift evolution of the characteristic absolute magnitude, M_B^*, of galaxies as measured in the luminosity function. This value has
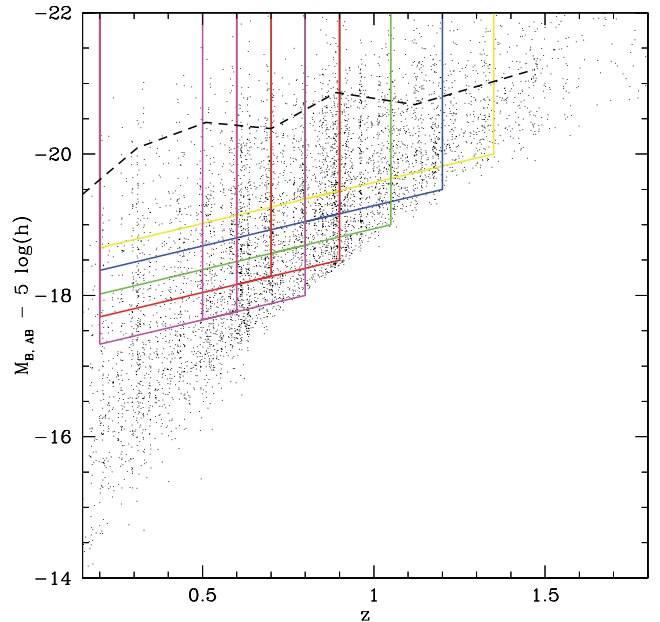

Figure 1. M_B for the VVDS galaxies at different redshifts. The solid coloured lines denote the various subsamples selected with properties mentioned in Table 1. The dashed line shows the observed evolution in M_B^*.

been determined using the luminosity function measurements obtained within the same sample by Ilbert et al. (2005).

An evolving luminosity threshold needs to be taken into consideration when comparing samples at different epochs, as it provides us with statistically similar samples at different redshifts, having similar evolved luminosities. Assuming that the global evolution of galaxies has as a main consequence to increase the global luminosity of galaxies, we follow the evolution of galaxies with similar properties on average. This falls within the boundaries of standard practice of galaxy evolution studies.

As our subsamples are nearly volume complete, and as we are using all types of galaxies together, we may follow the global increase in the halo mass of an average galaxy. However, we do recognize that this way of selecting galaxies does not guarantee to follow the exact same population with cosmic time. Unfortunately, there is no single prescription enabling to tag galaxies and exactly follow their precursors/descendants. Indeed, if this were possible it would be the solution to galaxy evolution. To try to quantify the impact of our selection on the average halo mass, we have used the Millennium Simulation. This will be further discussed in the next section.

Samples using a similar type of selection, i.e. using luminosity thresholds, have been extensively studied within a theoretical framework (Zehavi et al. 2005; Coil et al. 2006; Conroy et al. 2006; Zheng et al. 2007). The corresponding HOD parametrization requires fewer parameters to be fitted as compared to differential, luminosity-binned samples. However, this means that one is biased towards increasingly brighter galaxies at higher redshifts, simply due to the fact that the sample is selected in apparent magnitude. As can be seen in Fig. 1, there is a change of about 5 in the *B*-band absolute magnitude over the redshift bin $z \approx [0.1, 1.5]$. Table 1 shows the various properties of the subsamples along with their number densities. The galaxy number densities were computed by integrating the luminosity functions, derived by Ilbert et al. (2005) on the same galaxy sample and parametrized using Schechter functions. The evolution in the best-fitting Schechter parameters, M^*, ϕ^* and α were taken into consideration, thereby accounting for

Table 1. Properties of the different subsamples.

M_B^{thresh}	M_B^{low}	M_B^{high}	z range	$\bar{z}$	N_{gal}	$\bar{n}$ $(10^{-3}\,h^3\,\mathrm{Mpc}^{-3})$	M_B^{mean}	M_B^*
< -18.0	-17.31	-17.77	[0.2–0.6]	0.44	959	$25.81^{+4.29}_{-4.22}$	-17.61	-20.44
	-17.66	-18.00	[0.5–0.8]	0.66	1650	$26.48^{+6.43}_{-6.38}$	-17.86	-20.47
< -18.5	-17.69	-18.27	[0.2–0.7]	0.53	1281	$18.83^{+3.93}_{-3.74}$	-18.09	-20.39
	-18.16	-18.50	[0.6–0.9]	0.76	1673	$20.25^{+6.20}_{-5.90}$	-18.37	-20.80
< -19.0	-18.02	-18.71	[0.2–0.8]	0.59	1410	$13.79^{+3.53}_{-3.25}$	-18.50	-20.37
	-18.60	-19.00	[0.7–1.05]	0.88	1628	$15.23^{+5.98}_{-5.43}$	-18.85	-20.77
< -19.5	-18.35	-19.16	[0.2–0.9]	0.67	1541	$9.56^{+3.02}_{-2.68}$	-18.93	-20.56
	-19.04	-19.50	[0.8–1.2]	0.99	1526	$11.05^{+5.53}_{-4.73}$	-19.32	-20.76
< -20.0	-18.67	-19.48	[0.2–0.9]	0.67	1143	$6.77^{+2.39}_{-2.05}$	-19.25	-20.57
	-19.37	-20.00	[0.8–1.35]	1.05	1443	$7.31^{+4.54}_{-3.63}$	-19.76	-20.97

luminosity evolution. We estimated the errors on the number densities by propagating the errors on the Schechter parameters. M_B^{thresh} denotes the evolving absolute magnitude threshold at the highest redshift. For each M_B^{thresh} two samples were obtained, one at low redshift and another at higher redshift with brighter galaxies selected due to the evolving selection cut. The two samples overlap slightly in redshift in order to maximize the number of objects. M_B^{low} and M_B^{high} are the absolute magnitudes of the evolving cut at the lower and higher redshift limits, respectively, of the redshift range.

2.2 Studies with simulations

Ideally, we would like to follow statistically the same galaxy population with time in order to study the growth of the underlying dark matter halo mass. This is a tricky issue as it is difficult if not impossible to know the exact progenitors of a descendant galaxy population and how to select them. However, by taking care to follow the *exact population mix* down to a fixed absolute luminosity, we can minimize the bias in the average halo mass due to the presence/lack of faint or bright galaxies. As mentioned above, this is made possible by accurate measurements of galaxy evolution. In order to tackle this issue we use the milli-Millennium Simulation of galaxies having 270^3 particles in a box of $62.5\,\mathrm{Mpc}\,h^{-1}$ on its side (Springel et al. 2005). The simulations retain information on the progenitor trees of galaxies making it possible to make a comparison with volume-limited samples.

Let us select a galaxy sample at high redshift chosen with a luminosity cut-off in the B-band similar to what is done in the VVDS data, hereafter called the 'parent sample'. This sample is then evolved into two samples at lower redshift, a 'simulated sample' at the lower redshift, having a luminosity cut-off that is evolved and fainter (again similar to what we did in the data), and another sample that contains all the descendant galaxies at the same lower redshift (hereafter the 'descendant sample'). Doing a galaxy-to-galaxy match between the two samples would tell us how many galaxies in the simulated data set are actual descendants and therefore the same population followed through time and the effects on the underlying average halo mass. Table 2 shows the Millennium samples selected having roughly the same mean redshift and mean absolute magnitude, M_B, as in the VVDS data sample of Table 1.

We find that at worst 77 per cent of the $M < -20$ and at best 87 per cent of the $M < -18$ simulated luminosity-threshold sam-

Table 2. Simulated data sets versus descendants.

Sample	$\bar{z}$	M_B^{mean}	Avg. halo mass $(10^{10}\,\mathrm{M}_\odot\,h^{-1})$	Overlap per cent
Parent	0.69	-17.86	127.04	
Simulated	0.46	-17.61	164.84	
Descendant	0.46	-17.71	176.21	86.96
Parent	0.76	-18.37	135.56	
Simulated	0.51	-18.09	181.83	
Descendant	0.51	-18.17	199.49	84.03
Parent	0.90	-18.85	125.82	
Simulated	0.56	-18.50	192.06	
Descendant	0.56	-18.57	219.35	82.10
Parent	0.99	-19.32	125.60	
Simulated	0.69	-18.93	177.15	
Descendant	0.69	-19.05	202.82	80.43
Parent	1.08	-19.76	126.24	
Simulated	0.69	-19.25	191.36	
Descendant	0.69	-19.42	232.73	77.12

ple are actual descendants at lower redshifts. From Table 2 we can also study the effect of the selections on the underlying average halo mass. It can be seen that typically the underlying haloes in the descendant sample are heavier than those in the simulated sample. After taking a closer look at the descendant sample we noted that even though there are a larger number of fainter galaxies, there are also slightly more bright galaxies that lead to a slightly higher average magnitude. The combination of faint satellite galaxies residing in massive haloes and fewer galaxies of intermediate luminosity, likely lead to a descendant sample with more massive haloes and slightly brighter galaxies on average than the simulated sample. This possibly causes a lower overlap between the simulated and descendant samples for the brightest samples.

The Millennium Simulation shows that a growth in halo mass detected in the data would be underestimated with respect to what could be seen ideally. The underestimation in mass is of the order of roughly 10 per cent, and therefore a measure in the growth of mass of a halo can be mainly attributed to the hierarchical formation of structure and not due to the typology of the selection (taking into consideration the high overlap between the simulated and descendant samples).

2.3 The correlation function

The redshift–space correlation functions for the different luminosity-threshold samples have been computed via the Landy & Szalay (1993) estimator:

$$\xi(r_p, \pi) = \frac{N_R(N_R - 1)}{N_G(N_G - 1)} \frac{GG(r_p, \pi)}{RR(r_p, \pi)} - \frac{N_R - 1}{N_G} \frac{GR(r_p, \pi)}{RR(r_p, \pi)} + 1,$$

(1)

where N_G and N_R are, respectively, the total number of galaxies and randomly distributed points in the same survey. $GG(r_p, \pi)$ is the number of distinct galaxy–galaxy pairs with separations lying in the interval $(\pi, \pi + d\pi)$ in the radial direction and $(r_p, r_p + dr_p)$ perpendicular to the line of sight. Likewise, $RR(r_p, \pi)$ and $GR(r_p, \pi)$ are the number of random–random pairs and galaxy–random pairs, respectively, in the same interval.

In order to avoid redshift space distortions, $\xi(r_p, \pi)$ has been integrated along the line of sight to obtain the projected correlation function (Davis & Peebles 1983):

$$\omega_p(r_p) = 2 \int_0^\infty \xi(r_p, \pi) \, d\pi$$
$$= 2 \int_0^\infty \xi \left[\sqrt{r_p^2 + y^2} \right] \, dy,$$

(2)

where $\xi(r)$ is the real space correlation function with $r = \sqrt{r_p^2 + y^2}$. The measurements using the same sample impose a similar upper limit (Pollo et al. 2005, 2006; Meneux et al. 2006). Pollo et al. (2005) found that $\omega_p(r_p)$ is quite insensitive to π_{max} in the range of $15 < \pi_{max} < 25 \, \text{Mpc} \, h^{-1}$ for $r_p < 10 \, \text{Mpc} \, h^{-1}$. Too small a value for this limit would cause an underestimation of the small-scale power, and too large a value would introduce noise. After several experiments, the optimal value of $\pi_{max} = 20 \, \text{Mpc} \, h^{-1}$ has been adopted. The errors have been estimated using bootstrap resampling of the data, which consists of computing the variance of $w_p(r_p)$ in N_{real} bootstrap realizations of the sample. Each realization is obtained by randomly selecting a subset of galaxies from the data sample allowing for repetitions. A correction factor is then applied to account for the underestimation of the errors obtained using this technique. This correction factor has been calibrated on mock samples to match the ensemble error (accounting for cosmic variance) of the simulated mock samples (see Pollo et al. 2006).

3 ANALYTICAL MODELLING

3.1 The halo model

The analytical model is based on the halo model (see Cooray & Sheth 2002, for a review), here we will briefly mention the main ingredients. All mass is assumed to be bound up into dark matter haloes having a range of masses which in turn host galaxies.

In this model the power spectrum, $P(k)$, and/or correlation function, $\xi(r)$, of the galaxies (which are Fourier transform pairs) can be written as the sum of two terms. One that dominates on non-linear scales, smaller than the size of a halo, and the other term becoming significant on larger linear scales, known as the 1-halo and 2-halo terms, respectively. The 1-halo term arises from pairs of galaxies lying within the same halo, whereas pairs of galaxies lying in different haloes contribute to the 2-halo term. In Fourier space this can be written as

$$P(k) = P_{1h}(k) + P_{2h}(k),$$

(3)

where

$$P_{1h}^{gal}(k, z) = \frac{1}{\bar{n}_{gal}^2} \int_0^\infty dm \, n(m, z) \langle N_g(N_g - 1)|m\rangle \, |u(k|m)|^2,$$

$$P_{2h}^{gal}(k, z) = \left(\frac{1}{\bar{n}_{gal}} \int_0^{M_{max}} dm \, n(m, z) \langle N_g|m\rangle \, b(m, z) \, |u(k|m)| \right)^2$$
$$\times P_{lin}(k, z)$$

(4)

and $\bar{n}_{gal}$ is the number density of galaxies:

$$\bar{n}_{gal} = \int_0^\infty dm \, n(m, z) \langle N_g|m\rangle.$$

(5)

Here, $\langle N_g|m\rangle$ is the average number of galaxies occupying a halo of mass m, $u(k|m)$ is the halo density profile in Fourier space, $n(m, z)$ is the number density of haloes of mass m, $b(m, z)$ is the bias factor which describes the strength of halo clustering and $P_{lin}(k, z)$ is the power spectrum of the mass in linear theory all at a given redshift z. The upper limit of integration, M_{max}, approximately accounts for the halo exclusion effect (different haloes cannot overlap) by suppressing the 2-halo term at small scales. Following Zehavi et al. (2004), M_{max} is the mass of the halo with virial radius $r/2$. One can also calculate the 1-halo term for the correlation function exactly in real space, which is the approach we have taken. For more details we refer the reader to Berlind & Weinberg (2002). The 2-halo term has been computed in k-space and then Fourier transformed to obtain the correlation function. Then the projected correlation function is obtained as in equation (2). Similarly to the data the upper limit is chosen to be finite ($r_{max} = 20 \, \text{Mpc} \, h^{-1}$) in order to avoid noise caused by uncorrelated distant pairs.

We assume that the density profiles of haloes have the form described by Navarro, Frenk & White (1997), with a halo concentration parameter $c(M, z) = 11(M(z)/M_*(z))^{-0.13}$ to account for the definition of haloes as spheres enclosing 200 times the background density (Zehavi et al. 2005) and where $\sigma(M_*, z) = \delta_{sc}$ (σ and δ_{sc} are defined below). The halo abundances and clustering are described by the Sheth & Tormen (1999) parametrization:

$$\frac{m}{\bar{\rho}} n(m, z) \, dm = f(\nu) \, d\nu$$

$$= \frac{d\nu^2}{\nu^2} \sqrt{\frac{a\nu^2}{2\pi}} \exp\left(-\frac{a\nu^2}{2}\right) A[1 + (a\nu^2)^{-p}],$$

$$b(m, z) = 1 + \frac{a\nu^2 - 1}{\delta_{sc}} - \frac{2p/\delta_{sc}}{1 + (a\nu^2)^p},$$

$$\nu = \frac{\delta_{sc}}{\sigma(m, z)},$$

(6)

allowing us to write the background density as

$$\bar{\rho} = \int dm \, n(m, z) \, m,$$

(7)

with δ_{sc} being the critical density required for spherical collapse, extrapolated using linear theory to the present time ($= 1.686$, ignoring the weak cosmological dependence), $a \approx 0.71$, $p = 0.3$ and $A \approx 0.322$. $\sigma(m, z)$ is the rms value of the initial fluctuation field when smoothed with a top-hat filter and extrapolated to the present time using linear theory.

$$\sigma(m, z) = \sigma(m, 0) \frac{G(z)}{G(0)},$$

(8)

where G is the growth factor from Carroll, Press & Turner (1992).

3.2 The HOD models

We will consider two similar HOD models. The first one is based on the model used in Zehavi et al. (2005) (hereafter Z model) to

compare to the SDSS data, and is motivated by Kravtsov et al. (2004):

$$\langle N_g | m \rangle = 1 + \left(\frac{m}{M_1} \right)^\alpha \quad \text{for } m > M_{\min}$$

$$= 0 \qquad \qquad \text{otherwise.} \qquad (9)$$

The second model was proposed by Tinker et al. (2005, hereafter TWZZ model) and is given by

$$\langle N_g | m \rangle = 1 + \frac{m}{M_1} \exp\left(-\frac{M_{\text{cut}}}{m} \right) \quad \text{for } m > M_{\min}$$

$$= 0 \qquad \qquad \text{otherwise,} \qquad (10)$$

where $M_{\min}$ is the minimum mass for a halo to host one central galaxy, and M_1 is the mass of a halo hosting on average one satellite galaxy. The '1' represents one central galaxy placed at the centre of mass of the parent halo, and the satellite galaxies follow the underlying dark matter distribution. TWZZ model has been used to study the HOD for a range of redshifts and number densities and found to give results for the correlation function in good agreement with various redshift surveys in the range $z = [0–5]$ (Conroy et al. 2006).

Our purpose here will be to obtain the best-fitting HOD parameters for the two models, and compare the number-weighted halo masses and number of galaxies. We have decided to use these models in order to keep things simple and easy to interpret. Based on the statistics of the sample and the number of data points used, it is best to use HOD models with a minimal number of free parameters adapted to the science case at hand, i.e. for this paper, the average halo masses and number galaxies mentioned below. The main results that are obtained should remain essentially the same irrespective of the HOD model chosen.

A complementary approach would be to use modelling based on conditional luminosity functions (CLF) or conditional occupation numbers (CON; e.g. van den Bosch, Yang & Mo 2003; Yang, Mo & van den Bosch 2003; Cooray 2006). The present attempt is a first at using a large number of galaxy spectra at high redshift to study the evolutionary behaviour of a few properties pertaining to the galaxy and dark matter distribution. These 'few' properties are certainly not comprehensive, and this work can be seen as a starting point for more studies using the sample. Moreover, larger data samples from ongoing and upcoming redshift surveys will certainly provide grounds for extensive studies based on CLF/CON.

4 RESULTS

4.1 Results from VVDS

The different parameters were allowed to vary within the following ranges: $10 \leq \log(M_{\min}) \leq 15$, $10 \leq \log(M_1) \leq 15$, $10 \leq \log(M_{\text{cut}}) \leq 15$, $0.5 \leq \alpha \leq 2.0$. These limits represent reasonable constraints on the typical mass of a dark matter halo and the power-law slope. The minimum mass for a halo to host one central galaxy is usually $\geq 10^{11} h^{-1} M_{\odot}$ for low-redshift galaxies (Zehavi et al. 2005), and LBGs at high redshifts (Hamana et al. 2004). At the high-mass end, the brightest SDSS galaxy samples have $M_{\min} < 10^{14} h^{-1} M_{\odot}$. Taking into account our sampling having brightest samples of galaxies at high redshifts, in the hierarchical structure formation scenario this then represents an upper limit on the mass. On the other hand, M_1 has been found to be $\sim 23 M_{\min}$ (Zehavi et al. 2005). Furthermore, power-law slopes ≥ 1.5 are considered 'artificially high', which generally dominate brighter samples that have fewer satellite galaxies on average (Conroy et al. 2006). The number density obtained using equation (5) was restricted to lie within 3σ from the observed number density given in Table 1. The correlation functions for the different luminosity-threshold samples are shown in Fig. 2 along with the best fits for the two HOD models obtained with the MPFIT algorithm (Markwardt 2009) that uses the Levenberg–Marquardt technique (Moré 1978) to solve the non-linear least-squares problem using the full covariance matrix.
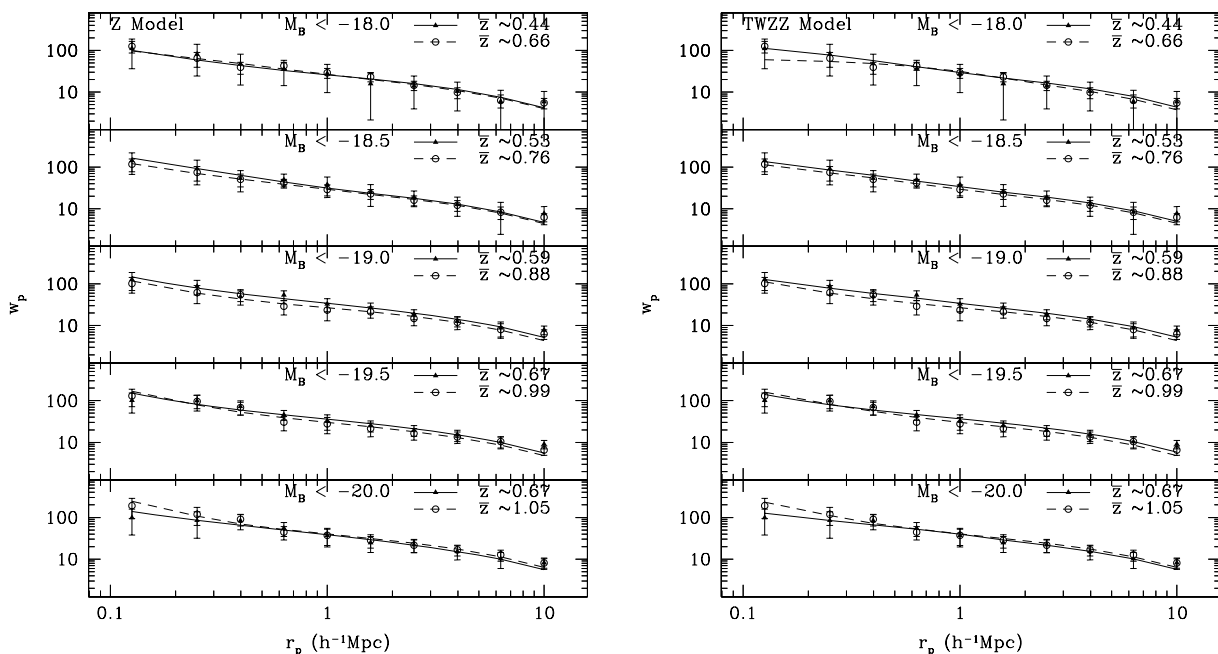

Figure 2. The correlation function for the various luminosity-threshold samples. The symbols and error bars denote the measurements from the VVDS-Deep. The lines present the best-fitting halo model for Z model of Zehavi et al. (2005) in the left-hand panel and for TWZZ model of Tinker et al. (2005) in the right-hand panel.

Table 3. Results for Z model.

M_B^{high}	$\log_{10} M_{min}$	$\log_{10} M_1$	α	$\log_{10}\langle M\rangle$	$\langle N\rangle$	χ^2/dof	$\bar{n}_{fit}$
< -17.77	11.05 ± 0.87	12.73 ± 1.00	0.99 ± 0.10	13.00 ± 0.13	1.21 ± 0.01	1.03	37.28
< -18.00	11.21 ± 0.18	13.03 ± 0.11	1.27 ± 0.08	12.97 ± 0.08	1.12 ± 0.01	1.35	26.29
< -18.27	11.37 ± 0.16	12.93 ± 0.06	1.11 ± 0.12	13.14 ± 0.14	1.22 ± 0.01	0.88	20.65
< -18.50	11.63 ± 0.19	13.31 ± 0.18	1.31 ± 0.09	12.98 ± 0.06	1.11 ± 0.02	0.52	11.16
< -18.71	11.88 ± 0.08	13.57 ± 0.10	1.33 ± 0.16	13.10 ± 0.08	1.09 ± 0.03	1.16	6.59
< -19.00	11.76 ± 0.08	13.39 ± 0.08	1.19 ± 0.24	12.88 ± 0.09	1.11 ± 0.03	0.84	8.53
< -19.16	12.06 ± 0.12	13.72 ± 0.10	1.43 ± 0.27	13.11 ± 0.08	1.08 ± 0.05	1.51	4.39
< -19.50	11.92 ± 0.16	13.43 ± 0.22	1.22 ± 0.25	12.94 ± 0.07	1.12 ± 0.04	1.24	5.99
< -19.48	12.06 ± 0.07	13.78 ± 0.04	1.66 ± 0.18	13.13 ± 0.06	1.06 ± 0.05	1.08	4.36
< -20.00	12.35 ± 0.11	13.80 ± 0.16	1.42 ± 0.41	13.09 ± 0.04	1.08 ± 0.10	0.78	2.17

Table 4. Results for TWZZ model.

M_B^{high}	$\log_{10} M_{min}$	$\log_{10} M_1$	$\log_{10} M_{cut}$	$\log(\langle M\rangle)$	$\langle N\rangle$	χ^2/dof	$\bar{n}_{fit}$
< -17.77	11.00 ± 0.15	12.54 ± 0.39	13.01 ± 2.07	13.09 ± 0.03	1.11 ± 0.01	1.19	38.00
< -18.00	11.45 ± 0.19	11.87 ± 0.71	14.93 ± 0.62	12.82 ± 0.05	1.01 ± 0.02	1.33	14.51
< -18.27	11.67 ± 0.13	13.03 ± 0.22	13.32 ± 0.75	13.12 ± 0.01	1.09 ± 0.02	0.75	10.06
< -18.50	11.62 ± 0.08	12.93 ± 0.08	13.26 ± 0.24	12.98 ± 0.01	1.08 ± 0.02	0.51	11.09
< -18.71	11.88 ± 0.09	13.22 ± 0.29	13.45 ± 0.74	13.10 ± 0.01	1.07 ± 0.04	1.16	6.40
< -19.00	11.74 ± 0.11	13.22 ± 0.15	12.62 ± 0.89	12.88 ± 0.02	1.09 ± 0.03	0.81	8.71
< -19.16	12.14 ± 0.11	13.47 ± 0.19	13.49 ± 0.61	13.12 ± 0.01	1.06 ± 0.06	1.42	3.67
< -19.50	11.90 ± 0.16	13.23 ± 0.35	12.73 ± 0.82	12.94 ± 0.02	1.11 ± 0.04	1.17	6.18
< -19.48	12.07 ± 0.05	13.15 ± 0.16	13.97 ± 0.25	13.13 ± 0.01	1.04 ± 0.05	0.97	4.18
< -20.00	12.32 ± 0.12	13.54 ± 0.45	13.21 ± 0.76	13.09 ± 0.02	1.07 ± 0.10	0.73	2.27

Tables 3 and 4 show the best-fitting parameters for the two different models obtained by a minimum χ^2 estimate, the value of the reduced χ^2, along with the average number-weighted halo masses and number of galaxies per halo defined as

$$\langle M\rangle = \frac{\int_0^\infty n(m)\langle N_g|m\rangle m \, dm}{\int_0^\infty n(m)\, dm},$$

$$\langle N\rangle = \frac{\int_0^\infty n(m)\langle N_g|m\rangle \, dm}{\int_0^\infty n(m)\, dm}. \tag{11}$$

The generalized χ^2 estimate is obtained the usual way adopting

$$\chi^2 = \sum_{i=0}^{n_{bin}} \sum_{j=0}^{n_{bin}} \left[w_p^{obs}(r_{p_i}) - w_p^{model}(r_{p_i})\right] C_{ij}^{-1} \left[w_p^{obs}(r_{p_j}) - w_p^{model}(r_{p_j})\right], \tag{12}$$

where n_{bin} is the number of bins and C_{ij} is the covariance of the values of w_p between the ith and jth bins.

The results obtained from both models and given in the tables are found to be in agreement (at least for comparable parameters), which is to be expected as the models are similar. In the case of TWZZ model the power-law exponent is kept constant and the number of satellites has a smooth, exponential cut-off. For example, in both cases the value for the minimum mass (M_{min}) is very similar if not the same. The power-law exponent for the Z model several times shows values of α that are quite high (>1.4). Artificially high values have been noticed in fits to simulations as well (Conroy et al. 2006) and occur for galaxy samples at high redshifts. The 1σ error bars on the parameters are obtained with the MPFIT algorithm.

Fig. 3 shows the number-weighted average halo mass, $\langle M\rangle$, versus the redshift. The symbols with error bars represent the various subsamples selected from the VVDS. The error bars are obtained based on error propagation formulas. The point at the lowest redshift ($z \sim 0.1$) is obtained from the SDSS using the best-fitting HOD parameters from Zehavi et al. (2005). The mass in this case was calculated using the Z model for the luminosity-threshold sample having the same $M - M^*$ difference as the samples at higher redshift in the VVDS (where the difference in the r band for the SDSS has been converted to the B band; Ilbert et al. 2005). It can be seen that the halo mass evolves and increases as one goes to lower redshifts. This is an indication of the halo mass growth due to the hierarchical aggregation of matter. We find that on average $\langle M\rangle$ increases by 90 per cent from redshift ~ 1 to ~ 0.5, showing that massive haloes have a rapid accretion phase quite late on, similar to what is expected from N-body simulations (Wechsler et al. 2002). As shown in Wechsler et al. (2002) the mass growth can be easily characterized by the form $M(z) = M_0 \, e^{-\beta z}$. The interesting comparison with the addition of low-redshift SDSS points gives a linear minimum χ^2 fit of $\beta \sim 1.94 \pm 0.10$ for the Z Model and $\beta \sim 2.09 \pm 0.04$ for the TWZZ model. This is to be compared to the predictions of the mass accretion history of haloes in N-body simulations and haloes generated through PINOCCHIO (Monaco, Theuns & Taffoni 2002; Wechsler et al. 2002; Li et al. 2007), where $\beta \sim 0.62$. One can argue that the direct comparison between data obtained from different rest-frame bands can be tricky and could in part lead to a slight boost in β, even though necessary care has been taken in converting to a common rest-frame band. The latter is reflected in the value obtained for β, using only the VVDS points leads to a smaller value [$\sim 1.54(1.07) \pm 0.13(0.57)$ for TWZZ (Z) model] albeit with larger error than that obtained from the extrapolation to smaller redshifts, but slightly more consistent with the results from simulations.

For samples at similar redshifts we can see that the number-weighted average halo mass increases with the luminosity threshold
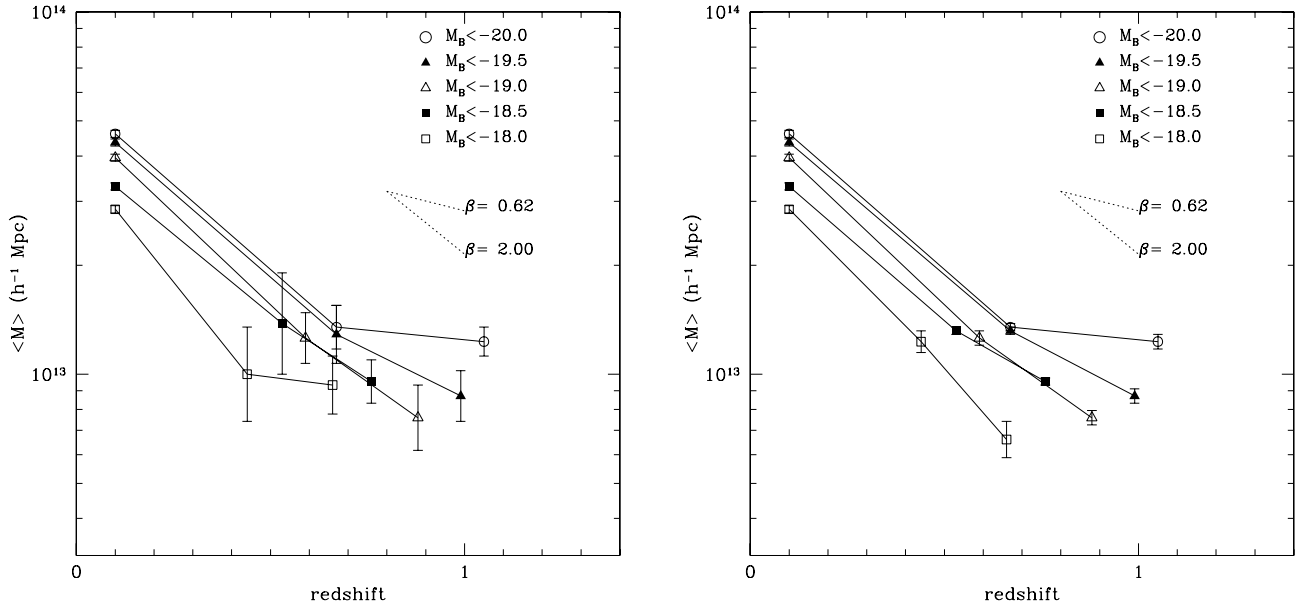
Figure 3. The evolution in the number-weighted average halo mass given by equation (11) for various luminosity-threshold samples is shown for the Z model (left-hand panel) and TWZZ model (right-hand panel). The symbols with error bars are obtained from the VVDS, whereas the low-redshift symbols at $z = 0.1$ with small error bars are from the SDSS. The mass growth can be characterized by $M(z) = M_0\,e^{-\beta z}$, with $\beta = 1.07 \pm 0.57$ (for the VVDS points), $\beta = 1.94 \pm 0.10$ (VVDS + SDSS points) in the case of the Z model, and $\beta = 1.54 \pm 0.13$ (for the VVDS points), $\beta = 2.09 \pm 0.04$ (VVDS + SDSS points) for the TWZZ model. The values of $\beta = 0.62$ and 2.00, respectively, represent the prediction from *N*-body simulations and the VVDS + SDSS samples.

of the sample reinforcing the notion that luminous galaxies occupy massive haloes. This is in agreement with results obtained from simulations (Conroy et al. 2006) and for LBGs (Lee et al. 2006; Ouchi et al. 2005).

Fig. 4 presents the evolution of the galaxy satellite fraction, or the average number of satellite galaxies. The illustrative reciprocal power-law behaviour of the data set shows relatively little change in the satellite fraction (always close to ~0.1 within 1σ) over the red-

shift range of $z = [0.5–1.0]$. Over $z = [0.1–0.5]$ there is a sharper increase by a factor of ~3 to the local SDSS value of ~0.3. The evolution is mainly accentuated by the SDSS points, although the two lowest redshift VVDS points for the case of the Z model do hint towards an increase with lower redshifts. It is possible that the sharper upturn is once again caused by the complicated comparison between two different data surveys. However, here again care has been taken to convert to the appropriate rest-frame band when
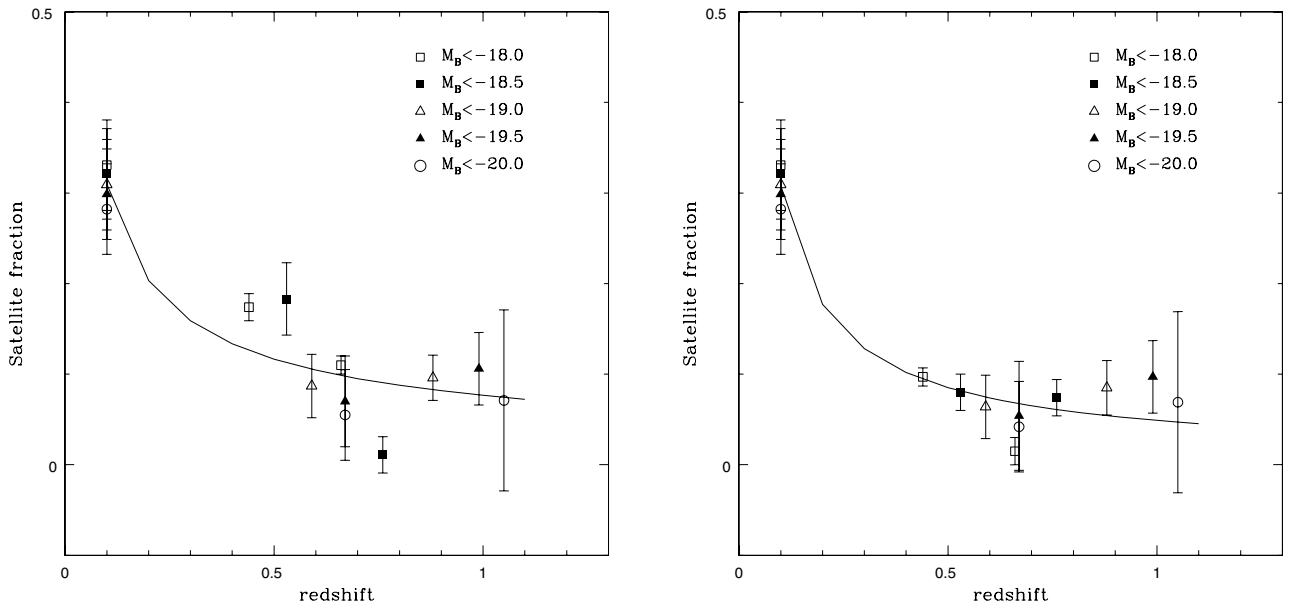

Figure 4. The evolution in the satellite fraction for various luminosity-threshold samples is shown for the Z model (left-hand panel) and TWZZ model (right-hand panel). The symbols with error bars are obtained from the VVDS, whereas the low-redshift symbols at $z = 0.1$ are from the SDSS. Simply for illustrative purposes, the curves show the reciprocal standard power-law behaviour, $y = 1/(ax^b)$, of the data, with $a = 13.05$ and $b = 0.61$ for the Z model, and $a = 20.41$ and $b = 0.79$ for the TWZZ model.
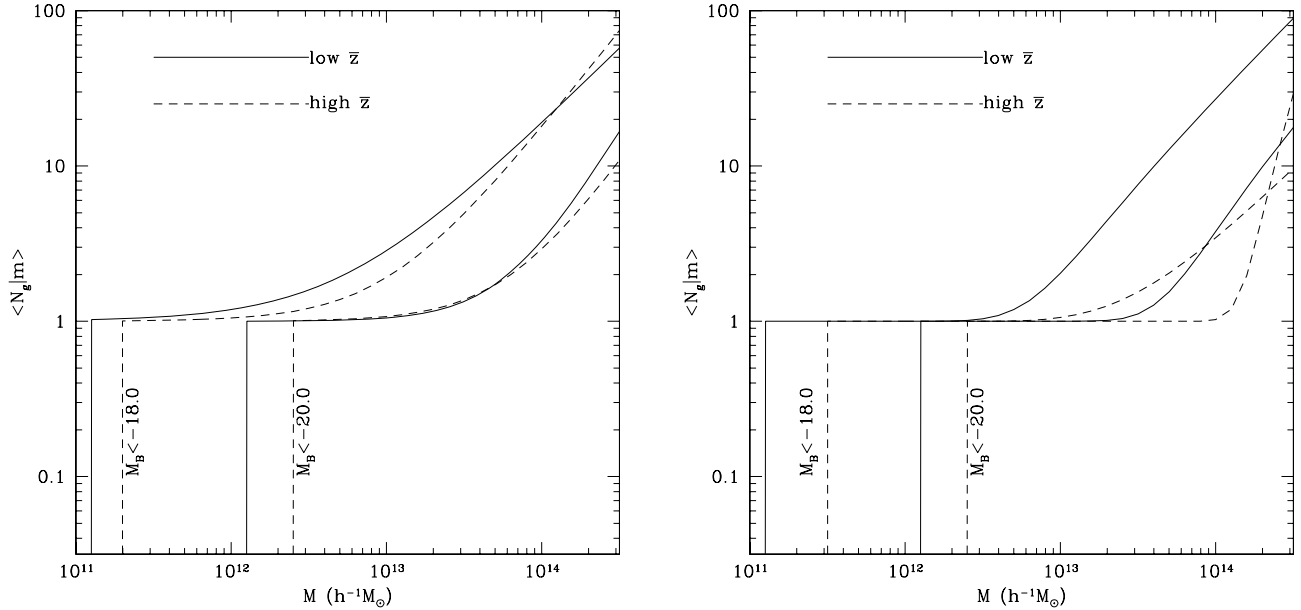
Figure 5. The evolution of the halo occupation for the extreme luminosity-threshold samples having $M_B < -18$, -20. The solid line corresponds to the lower redshift sample in each case, and the dashed line to the brighter sample at higher redshift both having the same evolved luminosity threshold (see Table 1). The solid lines correspond to $\bar{z} = 0.44$, 0.67 and the dashed lines to $\bar{z} = 0.66$, 1.05, respectively, for the samples with $M_B < -18$, -20. The left-hand panel depicts Z model and the right-hand panel TWZZ model.

making these comparisons and should not affect the overall trend. The increase in the satellite fraction as one goes to lower redshifts can be explained by the dynamical friction of subhaloes within their host haloes (Conroy et al. 2006). Subhaloes are more likely to remain intact within massive haloes, whereas in less massive haloes they are subject to more dynamical friction and can easily be destroyed. The dynamical friction becomes more/less efficient as a function of the relative masses of subhaloes to distinct haloes. This is to be compared to recent results obtained by Zheng et al. (2007) who find that the evolution of the satellite fraction follows a trend similar to what is seen here.

Fig. 5 shows the evolution in the halo occupation, $N_g(m)$, for the extreme luminosity-threshold samples obtained from the best-fitting parameters for the two models. Evidently, the minimum mass, M_{min}, increases with the luminosity of the sample as is found locally in the SDSS (Zehavi et al. 2005), again demonstrating that luminous galaxies occupy more massive haloes.

4.2 Comparison to SDSS

In this section we will compare to results for the same HOD model (Z model) as used in Zehavi et al. (2005). Fig. 6 shows the comparison between the masses of haloes that have at least one central galaxy (M_{min}) and one satellite galaxy (M_1) on average as a function of L_{thresh}/L_*, where the ratio is in the B band, and L_{thresh} is the luminosity threshold given in Table 1 (L_{thresh} and L_* are at similar redshifts). Here we will try to compare results obtained at different redshifts. For 40 per cent of the VVDS samples, M_{min} is similar to the local SDSS results within the error bars, with the rest of the VVDS samples having higher values of M_{min}. Generally, the VVDS samples exhibit more massive halo masses, M_1, required to host satellite galaxies than what is seen locally. The value for the power-law slope, α, is mostly similar to that for local galaxies, with the bright intermediate-redshift galaxies showing a higher slope.

We can see that generally the samples with higher values for α, also have higher values of M_1 and M_{min} than present-day galaxies.

It is interesting to note the M_1/M_{min} ratio, which is on average $\sim$45, rather high as compared to the value of $\sim$23 for the SDSS galaxies. A direct comparison and interpretation of these results is complicated as one is looking at two different surveys taken in different rest-frame bands. However, we can speculate that the high value of the ratio implies that the halo with one central galaxy needs to accrete roughly 45 times its mass in order to host a satellite galaxy. In other words, a halo of a given mass is likely to have fewer satellite galaxies at higher redshifts as opposed to a halo of the same mass observed locally.

5 DISCUSSION AND CONCLUSIONS

The comparison of analytical models and data provides useful information of how the distribution of galaxies depends on the underlying dark matter. Subsequently, the best-fitting parameters obtained as a result of this comparison provide physical information regarding the dark matter haloes and galaxies.

The size of the VVDS data set allows one to study, with a unique sample, the global change in the underlying halo properties of an average galaxy down to $z \sim 1$. We attempt to follow the evolution in some properties of a magnitude-selected sample, evolving the magnitude cut-off based on accurate measurements of galaxy evolution. We have presented results of the fitting of analytical halo models, incorporating simple HOD models with minimal number of free parameters, to data (in this case the projected two-point correlation function) from the VVDS survey. This allowed us to study the evolution of the average number weighted halo mass and satellite fraction.

On different scales there are contributions from central–satellite, satellite–satellite and central–central pairs of galaxies to the correlation function thereby providing constraints on the evolution of the galaxy satellite fraction. The evolution was obtained from data
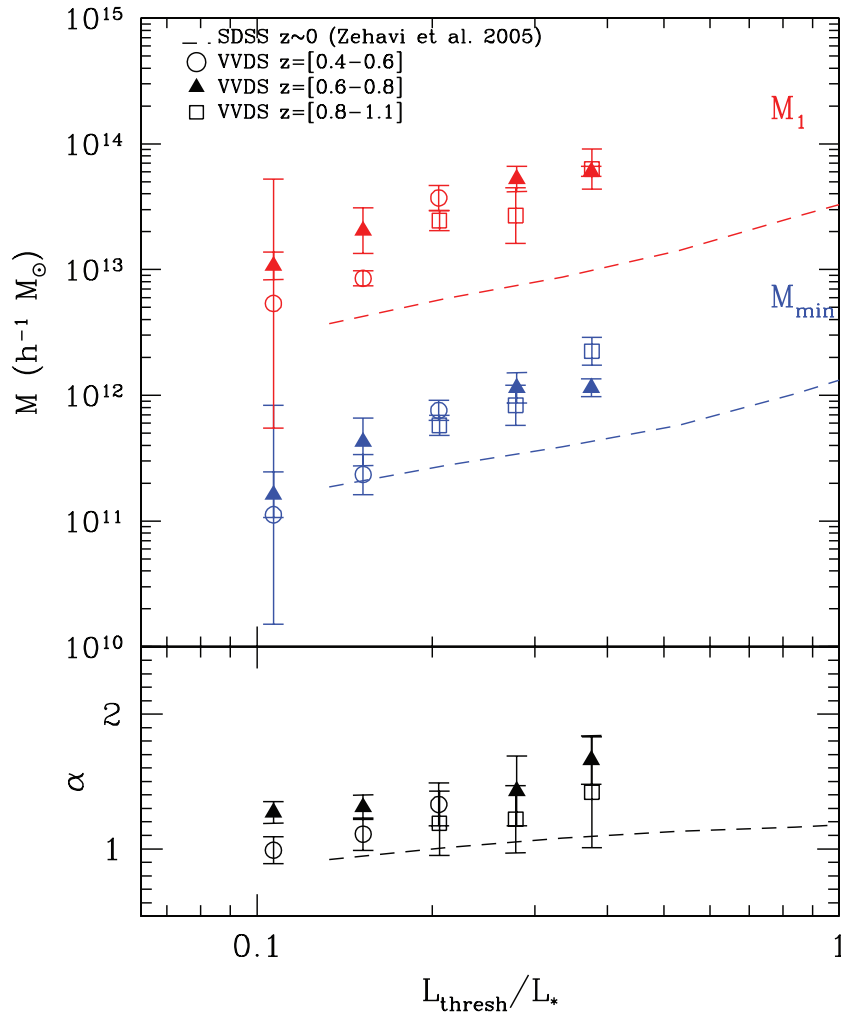
Figure 6. The best-fitting masses (M_{min}, M_1) and power-law slope α of haloes for Z model versus (L_{thresh}/L_*). The different symbols represent results for the VVDS, where each set of symbols correspond to samples lying in different redshift ranges (circles, solid triangles and empty squares represent samples having $z = [0.4–0.6]$, $[0.6–0.8]$, $[0.8–1.1]$, respectively). The superimposed dashed lines depict the SDSS.

observed in the same rest-frame band, and provides for simpler interpretations as compared to previous studies using data from different rest-frame bands. Various luminosity-threshold samples at different redshifts were selected and the corresponding best-fitting HOD parameters for two similar HOD models obtained. This is done in order to single out possible degeneracies and inconsistencies with the fitting procedure at high redshifts. On the whole, both models are in agreement with each other and show similar trends in evolution. The impact of our selection on the average halo mass is addressed using the Millennium Simulation. We find that a growth in halo mass as seen in the data could rather be an underestimation of ~10 per cent to what is seen in an 'ideal' sample containing all the descendants. Therefore a measure in the growth of mass of a halo can be mainly attributed to the hierarchical formation of structure and not due to the typology of the selection.

We find that the number-weighted average halo mass grows by ~90 per cent from redshift 1.0 to 0.5. This is the first time a growth in the underlying halo mass has been measured *at high redshifts* within a single data survey, and provides evidence for the rapid accretion phase of massive haloes. The mass accretion history follows the form given in Wechsler et al. (2002) with $M(z) = M_0 e^{-\beta z}$, where $\beta \sim 1.07 \pm 0.57 (1.54 \pm 0.13)$ when only the VVDS points were

used and $\beta \sim 1.94 \pm 0.10 (2.09 \pm 0.04)$ after including the SDSS data as reference points at low redshift and depending on the model used to obtain the best fits. The addition of the low-redshift SDSS points adds complications due to the addition of possible systematics by comparing data from two different rest-frame bands, even after conversion to a common fiducial band. We adopt the average value of $\beta \sim 1.3 \pm 0.30$ from the VVDS points when discussing a growth in halo mass, and found to be slightly higher than the results from *N*-body simulations.

If we express this result in terms of the expected halo mass at present times, $M_0 \simeq 10^{13.5} \, h^{-1} \, M_\odot$, such haloes appear to accrete $m \sim 0.25 M_0$ between redshifts of 0.5 and 1.0. Stewart et al. (2008) have shown that ~25 per cent (80 per cent) of $M_0 = 10^{13} \, h^{-1} \, M_\odot$ haloes experienced an $m > 0.3 M_0 \, (m > 0.1 M_0)$ merger event in the last 10 Gyr, this would translate into a $m > 0.1 M_0$ merger event over the redshift range $z = [0.5–1.0]$ for the high-mass haloes here. From merger rate studies one finds that 30 per cent of the stellar mass of massive galaxies with $10^{10} < M < 10^{11} \, M_\odot$ has been assembled through mergers since $z = 1$ (de Ravel et al. 2009, and references therein). The integrated stellar mass growth obtained can then be compared to the halo mass growth obtained here. For samples at similar redshifts we see that the average halo mass, $\langle M \rangle$,

generally increases with the luminosity threshold of the sample, with a very mild hint of a decreasing galaxy satellite fraction. This implies that galaxies in the faint sample show a stronger probability of being satellites in low-mass haloes as compared to bright galaxies in massive haloes.

We also find that the satellite fraction or average number of satellite galaxies appears to slowly increase over the redshift interval [0.5,1.0], but a stronger increase by a factor of ~ 3 over $z = [0.1, 0.5]$ is seen. This can be understood in terms of the dynamical friction that subhaloes hosting satellite galaxies encounter within their host haloes. The efficiency of dynamical friction depends on the relative subhalo to halo mass. Subhaloes experience more efficient dynamical friction in low-mass haloes, which can be thought of as progenitor haloes at high redshift. The subhaloes are continuously subjected to tidal stripping and gravitational heating within the dense environments and get eroded if not completely. As time evolves the halo accretes mass and undergoes mergers with other haloes. The subhaloes that form as remnants of halo mergers are now more likely to remain intact within the higher mass halo, in turn leading to a larger number of satellite galaxies in present-day haloes.

A comparison with the SDSS results shows a few interesting features. The value for M_{min}, which is the mass of a halo hosting at least one central galaxy on average, in 40 per cent of the luminosity-threshold VVDS samples is similar to values for local SDSS galaxies. Whereas, M_1 is generally higher for VVDS galaxies as compared to what is seen locally. The ratio of M_1/M_{min} is found to be considerably higher (almost a factor of 2) in the VVDS as compared to the SDSS results. This shows that in order to begin hosting satellite galaxies, haloes at high redshift need to accrete a larger amount of mass than is seen locally. Hence one would observe roughly twice as many local satellite galaxies than high redshift ones within the same evolved halo mass. This is another line of evidence in favour of the lower observed satellite fraction at high redshift and high local satellite fraction. This interpretation is highly simplified in light of the fact that the results have been obtained with data taken in different rest-frame bands.

In order to investigate further and better constrain the mass growth and evolution in the number of satellite galaxies per halo over a larger redshift range, one needs to have samples from the same survey at low redshifts. This can be done with samples from deeper and wider redshift surveys. Here we have concentrated on luminosity-threshold samples leading to a link between the luminosity of galaxies and the underlying dark matter distribution. The present paper can be seen as a precursor to many studies that can be carried out with larger samples than the VVDS, including CLF studies (e.g. van den Bosch et al. 2003, etc.), analyses with galaxy samples of different stellar masses (Zheng et al. 2007) etc. They will certainly add to the understanding of the vast pool of underlying dark matter properties and hopefully obtain tighter constraints on models of galaxy formation.

REFERENCES

Benson A., Cole S., Frenk C. S., Baugh C. M., Lacey C. G., 2000, MNRAS, 311, 793
Berlind A., Weinberg D. H., 2002, ApJ, 575, 587
Carroll S. M., Press W. H., Turner E. L., 1992, ARA&A, 30, 499
Coil A., Newman J. A., Cooper M. C., Davis M., Faber S. M., Koo D. C., Willmer C. N. A., 2006, ApJ, 644, 671
Connolly A. et al., 2002, ApJ, 579, 42
Conroy C., Wechsler R. H., Kravtsov A. V., 2006, ApJ, 647, 201
Conroy C. et al., 2007, ApJ, 654, 153
Cooray A., 2006, MNRAS, 365, 842
Cooray A., Sheth R. K., 2002, Phys. Rep., 372, 1
Davis M., Peebles P. J. E., 1983, ApJ, 267, 465
de Ravel L. et al., 2009, A&A, 498, 379
Gott J. R., Turner E. L., 1979, ApJ, 232, L79
Gunn J. E., Gott J. R., III, 1972, ApJ, 176, 1
Guzzo L., Iovino A., Chincarini G., Giovanelli R., Haynes M. P., 1991, ApJ, 382, L5
Hamana T., Ouchi M., Shimasaku K., Kayo I., Suto Y., 2004, MNRAS, 347, 813
Ilbert O. et al., 2005, A&A, 439, 863
Jenkins A. et al., 1998, ApJ, 499, 20
Kauffmann G., Colberg J. M., Diaferio A., White S. D. M., 1999, MNRAS, 303, 188
Kravtsov A. V., Berlind A. A., Wechsler R. H., Klypin A. A., Gottlober S., Allgood B., Primack J. R., 2004, ApJ, 609, 35
Landy S. D., Szalay A. S., 1993, ApJ, 412, 64
Lee K.-S., Giavalisco M., Gnedin O. Y., Somerville R. S., Ferguson H. C., Dickinson M., Ouchi M., 2006, ApJ, 642, 63
Le Fèvre O. et al., 2003, Messenger, 111, 18
Le Fèvre O. et al., 2004, A&A, 428, 1043
Le Fèvre O. et al., 2005a, A&A, 439, 845
Le Fèvre O. et al., 2005b, A&A, 439, 877
Li Y., Mo H. J., van den Bosch F. C., Lin W. P., 2007, MNRAS, 379, 689
McCracken H. et al., 2003, A&A, 410, 17
Magliocchetti M., Porciani C., 2003, MNRAS, 346, 186
Markwardt C., 2009, in Bohlender D., Dowler P., Durand D., eds, ASP Conf. Ser. Vol. 411. Astronomical Data Analysis Software and Systems XVIII. Astron. Soc. Pac., San Francisco, p. 251
Meneux B. et al., 2006, A&A, 452, 387
Monaco P., Theuns T., Taffoni G., 2002, MNRAS, 331, 587
Moré J., 1978, in Watson G. A., ed., Numerical Analysis, Vol. 630. Springer-Verlag, Berlin, p. 105
Navarro J., Frenk C., White S. D. M., 1997, ApJ, 490, 493
Ouchi M. et al., 2005, ApJ, 635, L117
Peacock J. A., 1997, MNRAS, 284, 885
Peebles P. J. E., 1974, A&A, 32, 197
Phleps S., Peacock J. A., Meisenheimer K., Wolf C., 2006, A&A, 457, 145
Pollo A. et al., 2005, A&A, 439, 887
Pollo A. et al., 2006, A&A, 451, 409
Sheth R. K., Tormen G., 1999, MNRAS, 308, 119
Springel V. et al., 2005, Nat, 435, 629
Stewart K., Bullock J. S., Wechsler R. H., Maller A. H., Zentner A. R., 2008, ApJ, 683, 597

Table A1. Projected correlation function with associated errors at different r_p for the different subsamples.

M_B^{low}	M_B^{high}	0.13	0.25	0.40	0.63	1.00	1.58	2.51	3.98	6.31	10.00	r_p
−17.31	−17.77	111.66	82.28	47.85	36.06	27.95	15.88	14.05	10.51	5.96	5.84	w_p
		37.60	29.03	16.56	10.86	9.12	6.86	5.05	3.48	2.51	2.29	σ
−17.66	−18.00	126.04	64.42	39.47	42.53	29.04	23.08	14.54	9.81	6.34	5.50	w_p
		30.37	19.46	9.63	7.13	5.98	4.16	2.84	2.19	1.70	1.20	σ
−17.69	−18.27	144.25	92.38	53.99	50.06	38.30	24.86	19.11	12.79	8.34	7.75	w_p
		38.60	27.52	14.16	9.26	9.81	6.69	3.95	3.11	2.94	1.80	σ
−18.16	−18.50	117.06	74.55	50.91	42.15	29.02	22.90	16.15	12.23	8.27	6.27	w_p
		30.44	21.94	13.42	6.66	6.67	4.67	3.38	2.72	2.11	1.08	σ
−18.02	−18.71	128.23	88.16	49.62	53.91	33.02	27.19	18.93	12.82	8.79	7.89	w_p
		44.93	25.76	14.40	10.92	8.82	5.67	3.95	2.71	2.65	1.41	σ
−18.60	−19.00	102.02	62.36	54.98	29.06	23.63	21.53	14.76	11.98	8.09	6.29	w_p
		32.39	22.12	13.33	8.43	8.13	5.01	3.70	3.07	2.37	1.23	σ
−18.35	−19.16	101.78	99.94	72.26	45.95	32.67	25.17	19.58	14.98	10.30	9.06	w_p
		39.40	27.35	20.75	9.48	9.99	5.75	4.33	3.53	2.56	1.57	σ
−19.04	−19.50	129.74	95.63	68.13	30.44	27.86	21.47	16.47	13.56	10.41	6.53	w_p
		44.85	30.38	17.90	8.77	8.93	6.04	3.99	3.20	2.39	1.28	σ
−18.67	−19.48	98.56	84.77	84.00	55.49	36.81	24.64	21.98	15.27	10.22	8.18	w_p
		46.76	40.82	25.60	15.59	12.05	7.89	5.94	4.37	3.25	1.95	σ
−19.37	−20.00	190.62	118.71	90.48	44.62	37.33	28.48	21.63	16.75	12.71	8.13	w_p
		73.55	42.16	21.57	12.33	13.63	7.79	5.60	3.70	2.94	1.61	σ

Tinker J. L., Weinberg D. H., Zheng Z., Zehavi I., 2005, ApJ, 631, 41

Totsuji H., Kihara T., 1969, PASJ, 21, 221

van den Bosch F. C., Yang X., Mo H. J., 2003, MNRAS, 340, 771

Wechsler R. H., Bullock J. S., Primack J. R., Kravtsov A. V., Dekel A., 2002, ApJ, 568, 52

Weinberg D. H., Davé R., Katz N., Hernquist L., 2004, ApJ, 601, 1

White S. D. M., Rees M. J., 1978, MNRAS, 183, 341

Yang X., Mo H. J., van den Bosch F. C., 2003, MNRAS, 339, 1057

Zehavi I. et al., 2004, ApJ, 608, 16

Zehavi I. et al., 2005, ApJ, 630, 1

Zheng Z., 2004, ApJ, 610, 61

Zheng Z., Coil A., Zehavi I., 2007, ApJ, 667, 760

APPENDIX A:

Here we present the table (Table A1) of values for the projected correlation function (w_p) and associated errors (σ) at different values of r_p (in units of Mpc h^{-1}) for the different subsamples mentioned in Table 1 in the main text. The values for w_p and σ are reported horizontally at the corresponding values for r_p in the top row.

This paper has been typeset from a TEX/LATEX file prepared by the author.